The Astrophysical Journal, 841:19 (13pp), 2017 May 20 https://doi.org/10.3847/1538-4357/aa704e

Small-scale Intensity Mapping: Extended Lyα, Hα, and Continuum Emission as a Probe of Halo Star Formation in High-redshift Galaxies

Lluís Mas-Ribas[1], Mark Dijkstra[1], Joseph F. Hennawi[2,3], Michele Trenti[4], Rieko Momose[5,6], and Masami Ouchi[5,7]
[1] Institute of Theoretical Astrophysics, University of Oslo, Postboks 1029, NO-0315 Oslo, Norway; l.m.ribas@astro.uio.no
[2] Max-Planck-Institut für Astronomie, Königstuhl 17, D-69117 Heidelberg, Germany
[3] Department of Physics, University of California, Santa Barbara, CA 93106, USA
[4] School of Physics, University of Melbourne, Parkville, VIC 3010, Australia
[5] Institute for Cosmic Ray Research, The University of Tokyo, 5-1-5 Kashiwanoha, Kashiwa, Chiba 277-8582, Japan
[6] Institute of Astronomy, National Tsing Hua University, 101 Section 2 Kuang-Fu Road, Hsinchu 30013, Taiwan
[7] Kavli Institute for the Physics and Mathematics of the Universe (WPI), The University of Tokyo, 5-1-5 Kashiwanoha, Kashiwa, Chiba 277-8583, Japan

Received 2017 March 7; revised 2017 April 25; accepted 2017 April 26; published 2017 May 18

Abstract

Lyα halos are observed ubiquitously around star-forming galaxies at high redshift, but their origin is still a matter of debate. We demonstrate that the emission from faint unresolved satellite sources, $M_{\rm UV} \gtrsim -17$, clustered around the central galaxies may play a major role in generating spatially extended Lyα, continuum (UV + VIS), and Hα halos. We apply the analytic formalism developed in Mas-Ribas & Dijkstra to model the halos around Lyman Alpha Emitters (LAEs) at $z = 3.1$, for several different satellite clustering prescriptions. In general, our UV and Lyα surface brightness profiles match the observations well at $20 \lesssim r \lesssim 40$ physical kpc from the centers of LAEs. We discuss how our profiles depend on various model assumptions and how these can be tested and constrained with future Hα observations by the *James Webb Space Telescope* (*JWST*). Our analysis shows how spatially extended halos constrain (i) the presence of otherwise undetectable satellite sources, (ii) the integrated, volumetric production rates of Lyα and LyC photons, and (iii) their population-averaged escape fractions. These quantities are all directly relevant for understanding galaxy formation and evolution and, for high enough redshifts, cosmic reionization.

Key words: galaxies: high-redshift – galaxies: star formation – Galaxy: formation – Galaxy: halo – infrared: galaxies

1. Introduction

Pioneering studies revealed the presence of diffuse Lyα emission in the halo of several star-forming galaxies (Møller & Warren 1998; Fynbo et al. 1999, 2001; Rauch et al. 2008). Nowadays, this faint emission is being proved to be nearly ubiquitous in galaxies at high redshift, $3 \lesssim z \lesssim 5$, by means of stacking analyses (Steidel et al. 2011; Matsuda et al. 2012; Feldmeier et al. 2013; Momose et al. 2014, 2016) and due to the sensitivity and spatial resolution improvement of instruments such as MUSE (Bacon et al. 2014). A clear understanding of the origin of these extended Lyα halos (LAHs; hereafter) is relevant because it yields information about the physical conditions of the circumgalactic medium (CGM) and, in turn, on the processes governing the formation and evolution of galaxies (Bahcall & Spitzer 1969).

The main mechanisms contributing to the existence of LAHs are (i) the cooling of gas accreted onto the galaxies and (ii) star formation. Star formation, additionally, can be divided into two processes: (i) The nebular Lyα radiation produced in the interstellar medium (ISM) diffusing outward to the CGM via *scattering* and (ii) the ionizing photons escaping the center of the galaxy which produce Lyα radiation in the neutral CGM via *fluorescence*.

The Lyα cooling radiation produced by the inflowing gas accreted onto the central galaxy has been investigated by several authors (Haiman et al. 2000; Kereš et al. 2005; Dekel & Birnboim 2006; Shull et al. 2009), but the significance of cooling is still difficult to predict accurately and remains uncertain (Fardal et al. 2001; Yang et al. 2006; Dijkstra & Loeb 2009; Faucher-Giguère et al. 2010; Cantalupo et al. 2012; Rosdahl & Blaizot 2012; Lake et al. 2015). The scattering of nebular Lyα photons produced in the H II regions of the central galaxy likely plays a major role in the observed Lyα surface brightness profiles at small distances from the center (a few tens of kiloparsecs; Laursen & Sommer-Larsen 2007; Laursen et al. 2009; Steidel et al. 2011; Zheng et al. 2011b; Wisotzki et al. 2016; Xue et al. 2017; F. Leclercq et al. 2017, in preparation) but at large impact parameters, scattering from the central galaxy alone usually cannot account for the totality of the observed emission (e.g., Lake et al. 2015, see also Dijkstra & Kramer 2012). Similarly, we demonstrated in Mas-Ribas & Dijkstra (2016) that the fluorescent effect of the central galaxy cannot explain the observed surface brightness profiles at distances $r \gtrsim 20$ physical kpc.

The nonlinear clustering of objects derived from the hierarchical Cold Dark Matter model of structure formation predicts that a significant fraction of the faint sources likely reside around more massive, brighter galaxies. Therefore, star-forming regions and galaxies surrounding the central galaxy (satellite sources) may provide additional contributions to the extended halos at large distances from the center, $r \gtrsim 30$ pkpc, via the nebular radiation produced “in situ” in their ISM, and/or inducing fluorescent emission in the CGM of the central galaxy (e.g., Shimizu & Umemura 2010; Matsuda et al. 2012; Lake et al. 2015; Momose et al. 2016, see Maiolino et al. 2017 for a recent detection of star formation within outflows). Although most of the satellites are probably too faint to be resolved individually, their overall collective emission may be detectable, similarly to the method of intensity mapping on large scales (e.g., Chang et al. 2010; Visbal & Loeb 2010;

Carilli 2011; Gong et al. 2011; Silva et al. 2013; Doré et al. 2014; Pullen et al. 2014; Croft et al. 2016; Li et al. 2016). We addressed the relevance of satellite sources in Mas-Ribas & Dijkstra (2016), accounting for the clustering of ionizing radiation, which, in turn, yields to enhanced fluorescent Lyα emission. Our results demonstrated that fluorescence alone cannot explain the observed profiles, but its contribution can be up to $\sim$50% out to $r \sim 30$ pkpc if conditions of a high escape fraction of ionizing photons and a cold gas covering factor are accomplished.

In the present work, we focus on the nebular emission ("in-situ" production) from the satellite sources. This analysis is important because, as we will demonstrate, we are able to reproduce the observed Lyα and UV surface brightness profiles, which supports the notion that faint satellite sources can explain the extended LAHs. We self-consistently also predict Hα and continuum surface brightness profiles for different models and parameters, which will be testable with future *JWST* observations. We show how the observations of Hα surface brightness profiles will serve to clearly distinguish between the mechanisms that give rise to spatially extended emission and will place constraints on halo star formation, in addition to the current UV measurements.

Obtaining tighter constraints to the presence of radiation sources in the halo of more massive galaxies allows for assessing the important role that faint objects played in the total cosmic photon budget (see, e.g., Nestor et al. 2011, 2013; Alavi et al. 2014; Garel et al. 2016) and, for high enough redshifts, their contribution to the reionization of the universe (Kuhlen & Faucher-Giguère 2012; Robertson et al. 2013). Interestingly, Croft et al. (2016) recently reported an excess of Lyα emission resulting from their cross-correlation between Lyα surface brightness and quasars from the Sloan Digital Sky Survey III (SDSS-III; Eisenstein et al. 2011) Baryon Oscillation Spectroscopic Survey (BOSS; Dawson et al. 2013). Croft et al. (2016) argued that if their measured Lyα emission is driven by star formation, this would result in a star formation rate density $\sim$30 times larger than what is obtained from Lyman Alpha Emitter (LAE) surveys, although consistent with dust-corrected UV continuum analyses. The star formation scenario, however, needs to invoke an escape fraction for Lyα $\sim$100% and strong radiative transfer effects. Our work can be viewed as a complementary experiment at smaller scales, where we "cross correlate" deeper Lyα intensity images with LAEs.

We perform calculations considering the spatially extended emission observed around LAEs at redshift $z = 3.1$, which allows a comparison with the results by Momose et al. (2014) and Matsuda et al. (2012). Our paper is structured as follows. In Section 2, we detail the formalism and adopted values for the parameters in the calculation of the surface brightness profiles for the continua, Hα and Lyα. We present the results for several models in Section 3, and provide a discussion in Section 4, before concluding in Section 5. Appendix A addresses the implications of the luminosity function (LF) parameter values in terms of the spatial and luminosity distribution of satellite sources around the central galaxy. In Appendix B, we detail the calculations of the signal-to-noise ratio (S/N) for our predicted observations with *JWST*.

We assume a flat ΛCDM cosmology with values $\Omega_\Lambda = 0.7$, $\Omega_\mathrm{m} = 0.3$, and $H_0 = 68$ km s^{-1} Mpc^{-1}.

2. Formalism

We present a simple analytic formalism that works with integrated properties of the entire emitting population, which allows the circumvention of the modeling of individual sources when calculating the surface brightness profiles.

We demonstrated in Mas-Ribas & Dijkstra (2016) that the fluorescent radiation from a central galaxy with SFR $\sim 10\,M_\odot$ yr^{-1} only dominates at distances $\lesssim$20–30 pkpc from the center and at a level that strongly depends on the characteristics of the circumgalactic gas. In addition, at such small distances, the profile of the central galaxy is significantly driven by the point-spread function of the instrument (Momose et al. 2014). Owing to these uncertainties, here we ignore the central galaxy and limit our calculations to distances >10 pkpc.

We use a similar formalism to that applied in Mas-Ribas & Dijkstra (2016), to which we refer the reader for details. Briefly, the Lyα and Hα surface brightness at impact parameter b equals

$$\mathrm{SB}_x(b) = \frac{2}{(1+z)^4}\int_b^{R_\mathrm{max}^\alpha} \bar{\epsilon}_x^\mathrm{sat}[1+\xi_x(r)]f_\mathrm{esc}^x \frac{rdr}{\sqrt{r^2-b^2}}, \tag{1}$$

where "x" stands for Lyα or Hα. The factor $(1+z)^{-4}$ accounts for the surface brightness dimming. The factor $\bar{\epsilon}_x^\mathrm{sat}$ denotes the integrated volume emissivity in satellite galaxies (see Section 2.1), the term $[1+\xi_x(r)]$ denotes the boost in emissivity due to the clustering of sources around the central galaxy (see Section 2.2), and f_esc^x denotes the escape fraction (see Section 2.3). Finally, the value for the upper limit of the integral extends to infinity for the Abel transformation used above, but we limit its value accounting for the line shift due to the expansion of the universe as

$$R_\mathrm{max}^\alpha = \frac{1}{2}\frac{c}{H(z)}\frac{d\nu_\alpha}{\nu_\alpha(z)}, \tag{2}$$

where $H(z)$ denotes the Hubble parameter at a given redshift, c is the speed of light, and $d\nu_\alpha/\nu_\alpha = 0.02$ accounts for the line shift for apertures in narrowband surveys of $\sim$100 Å, e.g., Matsuda et al. (2012). This approach implies $R_\mathrm{max}^\alpha \sim 3$ pMpc, but we have tested that our results show only differences of a factor of $\sim$2 at large distances, $r \gtrsim 80$–100 pkpc, when setting the upper limit within the range 300 pkpc $< R_\mathrm{max}^\alpha <$ 5 pMpc.

We calculate the UV surface brightness at 1500 Å rest frame as

$$\mathrm{SB}_\mathrm{UV}(b) = \frac{2}{(1+z)^3} \times \int_b^{R_\mathrm{max}^\mathrm{UV}} \bar{\epsilon}_\mathrm{UV}^\mathrm{sat}[1+\xi_\mathrm{UV}(r)]f_\mathrm{esc}^\mathrm{UV} \frac{rdr}{\sqrt{r^2-b^2}}, \tag{3}$$

where we use the parameters for UV radiation and multiplied Equation (1) by $(1+z)$, since the UV surface brightness is measured as a flux *density* (in units of inverse frequency) per unit solid angle.

We compute the surface brightness for the visible continuum (VIS) as

$$\mathrm{SB}_\mathrm{VIS}(b) = \frac{(1+z)}{\mathrm{EW}_{\mathrm{H}\alpha}}\frac{\lambda_{\mathrm{H}\alpha}^2}{c}\mathrm{SB}_{\mathrm{H}\alpha}(b). \tag{4}$$

We derive the VIS emission using the Hα equivalent width because visible radiation is not commonly used as a star formation estimator, therefore not providing a relation between star formation and luminosity at a specific wavelength, unlike Lyα, Hα, and UV in Equation (6) (see Kennicutt & Evans 2012, for a complete review). We assume a flat spectrum around Hα and a line equivalent width $\mathrm{EW_{H\alpha}} = 300$ Å (rest frame; e.g., Mármol-Queraltó et al. 2016, and references therein). In Equation (4), $\lambda_{\mathrm{H}\alpha}$ and c represent the Hα wavelength at rest and the speed of light, respectively, applied to obtain the surface brightness in units of inverse frequency. For completeness, we will also explore the ranges $450 \geqslant \mathrm{EW_{H\alpha}}\,[\text{Å}] \geqslant 150$ and $700 \geqslant \mathrm{EW_{H\alpha}}\,[\text{Å}] \geqslant 50$.

2.1. Volume Emissivity, $\bar{\epsilon}_x^{\mathrm{sat}}$

The integrated volumetric emissivity (i.e., volume emissivity) in faint satellites is given by

$$\epsilon_x^{\mathrm{sat}} = C_x \rho_{\mathrm{SFR}}^{\mathrm{sat}}, \tag{5}$$

where $\rho_{\mathrm{SFR}}^{\mathrm{sat}}$ denotes *the star formation rate density in faint satellites*. We are interested in the contribution to the star formation rate density from sources fainter than $M_{\mathrm{UV}} \equiv M_{\mathrm{UV}}^{\mathrm{sat}} = -17$, which corresponds roughly to the minimum UV luminosity of unlensed galaxies that can be detected directly (e.g., Bouwens et al. 2015; Finkelstein et al. 2015). For a UV LF with a faint-end slope $\alpha = -1.7\,(-1.5)$, this approach translates to extrapolating the LF to $M_{\mathrm{UV}} \sim -12$ ($M_{\mathrm{UV}} \sim -10$) (Kuhlen & Faucher-Giguère 2012; Alavi et al. 2016; Lapi et al. 2017; Livermore et al. 2017). The integrated cosmic star formation rate density in the *observed population* of star-forming galaxies is $\rho_{\mathrm{SFR}} \sim 0.1\,M_\odot\,\mathrm{yr^{-1}\,cMpc^{-3}}$ at $z \sim 3$ (see, e.g., Hopkins & Beacom 2006; Bouwens et al. 2015; Khaire & Srianand 2015; Robertson et al. 2015). We assume that $\rho_{\mathrm{SFR}}^{\mathrm{sat}} = \rho_{\mathrm{SFR}}$, for simplicity. This assumption depends in detail on the faint-end slope of the UV LF at $M_{\mathrm{UV}} > M_{\mathrm{UV}}^{\mathrm{sat}}$, on $M_{\mathrm{UV}}^{\mathrm{sat}}$ itself, and the UV magnitude down to which we integrate this LF. The precise value for $\rho_{\mathrm{SFR}}^{\mathrm{sat}}$ is, therefore, highly uncertain, and our results scale linearly with the value for this parameter. The constant C_x represents the standard conversion factor from SFR into UV luminosity density and Hα and Lyα luminosities, and is given by

$$C_x = \begin{cases} 1.30 \times 10^{42}\ \frac{\mathrm{erg\ yr}}{\mathrm{s}\ M_\odot} & (\mathrm{Ly}\alpha); \\ 1.26 \times 10^{41}\ \frac{\mathrm{erg\ yr}}{\mathrm{s}\ M_\odot} & (\mathrm{H}\alpha); \\ 8.00 \times 10^{27}\ \frac{\mathrm{erg\ yr}}{\mathrm{s}\ M_\odot\ \mathrm{Hz}} & (\mathrm{UV}). \end{cases} \tag{6}$$

The conversion factor for the UV continuum comes from Madau et al. (1998) and from Kennicutt (1998) for Hα. We obtain the conversion factor for Lyα from Hα, assuming the common $L_{\mathrm{Ly}\alpha} = 8.7 L_{\mathrm{H}\alpha}$ ratio (Brocklehurst 1971; Barnes et al. 2014; Dijkstra 2014), which assumes case-B recombination. We caution that these conversion factors, especially for Lyα, can vary depending on the metallicity, initial mass function (IMF), and ages of the stellar population (Raiter et al. 2010; Mas-Ribas et al. 2016). Additionally, the value of $C_{\mathrm{Ly}\alpha}$ strongly depends on the Lyα rest-frame equivalent width of the sources. We will demonstrate in Section 4.1 that accounting for this dependence over the faint satellite population has a significant impact on the results.

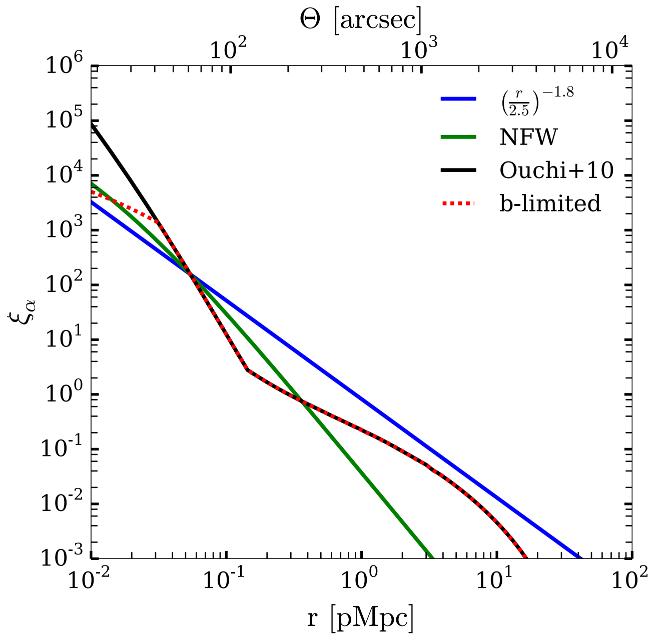

Figure 1. Lyα emission correlation functions as a function of distance from the central galaxy for different clustering models. The solid black line denotes our fiducial model, derived by extrapolating observational constraints on the scale-dependent bias by Ouchi et al. (2010). The dashed red curve displays the same model, but with the bias limited to a value 10 (the maximum value inferred by Ouchi et al. 2010) . The blue line indicates the common power-law clustering of LAEs at redshift $z \sim 3$. The green line denotes the NFW profile (see the text).

2.2. Clustering of Emission, $[1 + \xi_x(r)]$

The cross-correlation function of emission around LAEs is proportional to the matter density field and can be written as $\xi_x(r) = b_x(r) b_{\mathrm{LAE}}(r) \xi(r)$. The term $\xi(r)$ denotes the nonlinear dark matter correlation function obtained using CAMB (Lewis et al. 2000). The terms $b_{\mathrm{LAE}}(r)$ and $b_x(r)$ are the distance-dependent LAE and emission biases, respectively. We discuss these terms below.

2.2.1. The LAE bias, $b_{LAE}(r)$

Following Mas-Ribas & Dijkstra (2016) (see their Appendix B for details) our fiducial model (*solid black line* in Figure 1) adopts $b_{\mathrm{LAE}}(r)$ based on observations by Ouchi et al. (2010), who measured $b_{\mathrm{LAE}}(r)$ to increase to $b_{\mathrm{LAE}}(r) \sim 10$ down to $r \sim 20$ pkpc. We tested in our previous work that using this clustering we obtained an overdensity $\delta_{\mathrm{LAE}} \sim 1.5$, averaged over a radial distance of 2 Mpc h^{-1} from the central galaxy, consistent with the values reported by Matsuda et al. (2012). To quantify how much our results depend on extrapolating $b_{\mathrm{LAE}}(r)$ down to smaller scales, we have also repeated our calculations, but limiting the $b_{\mathrm{LAE}}(r)$ to a maximum value of 10. This model is represented in Figure 1 as the dotted red line. In addition, the observational uncertainties reported by Ouchi et al. (2010) for the bias at $r \sim 20$ kpc are of the order $\sim$50%, consistent at a 2σ level with the bias obtained assuming a power-law correlation function. Owing to these large uncertainties for the bias at small scales, we also explore other clustering prescriptions in Section 2.2.3 below.

2.2.2. Emission Bias, $b_x(r)$

The term $b_\alpha(r)$ expresses the distance-dependent bias of the Lyα emission, which we assume to differ from that of LAEs by a constant, i.e., $b_\alpha(r) = k\, b_{\rm LAE}(r)$. The bias $b_\alpha(r)$ represents the Lyα luminosity-weighted average of the entire satellite population. Its value thus depends on the faint-end slope of the Lyα LF ($\alpha_{{\rm Ly}\alpha}$, which is likely steeper than the UV LF; see, e.g., Gronke et al. 2015; Konno et al. 2016), although, as long as $\alpha_{{\rm Ly}\alpha} > -2$, we expect that the bias is set by the most luminous satellites with $M_{\rm UV} \sim M_{\rm UV}^{\rm sat} = -17$. Gronke et al. (2015) have shown that observational constraints on $M_{\rm UV}$-dependent Lyα equivalent width (EW) PDFs imply that the faintest LAEs ($L_{{\rm Ly}\alpha} \sim 10^{42}$ erg s^{-1}) are associated with galaxies with $M_{\rm UV} \sim -17.5$ (see their Figure 3). This result suggests that the UV-brightest satellites may cluster like LAEs, with $k \sim 1$, although fainter sources might present values $k > 1$. Croft et al. (2016) argue that $b_\alpha(r)$ might be further boosted by radiative transfer effects due to the resonant nature of the Lyα radiation (e.g., Zheng et al. 2011a). To be conservative, we adopt $k = 1$ in our fiducial model.[8]

Our fiducial model assumes that for both, UV and Hα emission, we have $b_{\rm UV}(r) = b_{{\rm H}\alpha}(r) = b_\alpha(r) = b_{\rm LAE}(r)$, i.e., $k = 1$. This choice is motivated by the discussion above, while noticing that radiative transfer cannot further enhance k in these cases. Our predicted surface brightness profiles again scale linearly with k.

2.2.3. Alternative Clustering Prescriptions

We consider two alternative clustering prescriptions:

1. The distribution of satellites follows that of dark matter in a Navarro–Frenk–White (NFW) profile (Navarro et al. 1997), normalized to be the same as the other clustering estimators at $r \sim 60$ pkpc (similar to the value of the virial radius for the central galaxy). This model is represented by the green line in Figure 1. The density profile in the NFW model equals

$$\rho(r) = \frac{\delta_c \rho_c(z)}{r/r_s(1 + r/r_s)^2}, \tag{7}$$

where $\rho_c(z)$ is the critical density of the universe at redshift z, δ_c is the characteristic overdensity and r_s is the scale radius of the dark matter halo. The overdensity δ_c can be expressed as

$$\delta_c = \frac{\Delta}{3}\frac{c_{\rm NFW}^3}{\log(1 + c_{\rm NFW}) - c_{\rm NFW}/(1 + c_{\rm NFW})}, \tag{8}$$

where $\Delta = 18\pi^2$ is the density contrast from Bryan & Norman (1998) and $c_{\rm NFW} = 4$ is the concentration parameter at $z = 3.03$ from Zhao et al. (2009). We obtain the scale radius from the expression $c_{\rm NFW} \equiv r_h/r_s$, where r_h is the halo virial radius, computed as

$$r_h = \left(\frac{3M_h}{4\pi\Delta\rho_c(z)}\right)^{1/3}. \tag{9}$$

This expression emerges from considering that the mean density of the halos within the virial radius is $\Delta\rho_c(z)$ (Sadoun et al. 2017). We have assumed an LAE halo mass $\log M_h = 11.5\, M_\odot$, consistent with the observed range of LAE masses in Ouchi et al. (2010).

2. We extrapolate the common LAE power-law two-point correlation function, with scale length $r_0 = 2.5$ Mpc h^{-1} and power-law index $\alpha_c = -1.8$ (e.g., Gawiser et al. 2007; Kovač et al. 2007; Ouchi et al. 2003, 2010; Guaita et al. 2010; Bielby et al. 2016) down to small scales. This clustering profile is denoted by the blue solid line in Figure 1. The power-law function presents differences with our fiducial model at distances above ~60 pkpc and at tens of pkpc from the center. In this last region is where the nonlinear clustering effects, not captured by the power-law, are important, therefore higher values for the fiducial function are expected.

2.3. Escape Fraction, $f_{\rm esc}^x$

The Lyα escape fraction, $f_{\rm esc}^{{\rm Ly}\alpha}$, has been constrained observationally to be $f_{\rm esc}^{{\rm Ly}\alpha} \sim 20\%$ at $z \sim 3$ from the Lyα and UV LFs (e.g., Blanc et al. 2011; Hayes et al. 2011) and from Lyα and star formation analysis (Dijkstra & Jeeson-Daniel 2013). However, we caution that all of the observations have constrained the "effective" escape fraction, which denotes the fraction of Lyα photons that reaches the observer. As mentioned previously, in some models, *all* Lyα photons escape from the ISM, but then scatter in the CGM/IGM to form halos (in these same models, Lyα radiative transfer causes $k > 1$). These photons would not have been considered in traditional measurements of Lyα LFs (up to a fraction 40% to $\gtrsim$90% of the total Lyα flux, as argued by Wisotzki et al. 2016, see also Drake et al. 2016) and, therefore, would not be considered for current observational constraints on $f_{\rm esc}^{{\rm Ly}\alpha}$. Also, there is observational evidence that the Lyα escape fraction increases toward lower UV luminosities (e.g., Japelj et al. 2017, see also Dijkstra et al. 2016 and references therein). While observations find $f_{\rm esc}^{{\rm Ly}\alpha} \sim 20\%$, we consider this value to likely be a lower-limit and we adopt the range $0.1 \leqslant f_{\rm esc}^{{\rm Ly}\alpha} \leqslant 1.0$ throughout, with a fiducial value $f_{\rm esc}^{{\rm Ly}\alpha} = 40\%$.

We adopt the same range and conservative fiducial value for UV and Hα escape fractions. We generally expect that $f_{\rm esc}^{\rm UV} \geqslant f_{\rm esc}^{{\rm Ly}\alpha}$ because UV photons are not affected by radiative transfer effects, i.e., resonant scattering that increases the chance to be destroyed by dust (see, e.g., Figure 7 in Garel et al. 2015). The escape fraction of Hα can be even larger than that of UV due to the wavelength dependence of the dust extinction curve (see, e.g., Pei 1992; Calzetti et al. 1994, 2000; Gordon et al. 2003).

3. Surface Brightness Profiles

We present the resulting surface brightness profiles below. It is important to keep in mind that these results are degenerate in the product of emissivity, escape fraction, and bias, $\bar{\epsilon}_x^{\rm sat} f_{\rm esc}^x\, b_x$, where x refers to UV, Hα, and Lyα.

3.1. Lyα

The left panel in Figure 2 shows the predicted Lyα surface brightness profile at $r > 10$ pkpc. The black solid line denotes the fiducial model, and the shaded areas indicate the range of surface brightness profiles we get by varying $0.2 \leqslant f_{\rm esc}^{{\rm Ly}\alpha} \leqslant 0.7$

---

[8] It is worth pointing out that the value of k formally cannot be chosen independently of the escape fraction (see Section 2.3); a high k value implies that radiative transfer in the CGM/IGM is important. In order to reproduce the observed Lyα LFs of LAEs, one then requires that $f_{\rm esc}^{{\rm Ly}\alpha} \sim 1$ (see Zheng et al. 2010).

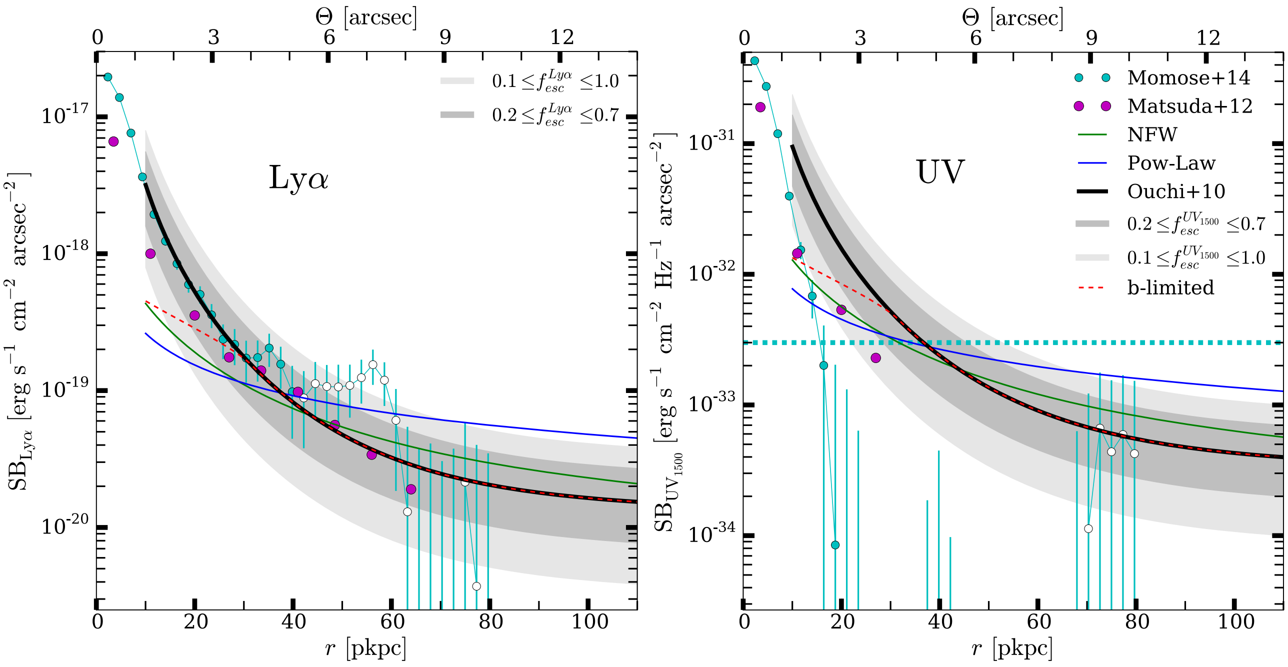

Figure 2. Left panel: radial Lyα surface brightness profiles with physical distance from the central galaxy for different models. Lines and colors refer to the same models as in Figure 1. Magenta points denote an estimation of the data for the LAE overdensity range $2.5 < \delta_{\rm LAE} < 5.5$ in Matsuda et al. (2012). The cyan dots and bars represent the mean values and uncertainties from the observations at $z = 3.1$ by Momose et al. (2014), respectively. White dots indicate the regions where the measurements are not reliable due to systematic effects. The fiducial model is denoted by the solid black line considering $f_{\rm esc}^{\rm Ly\alpha} = 0.4$, and the two shaded areas display the regions $0.2 \leqslant f_{\rm esc}^{\rm Ly\alpha} \leqslant 0.7$ and $0.1 \leqslant f_{\rm esc}^{\rm Ly\alpha} \leqslant 1.0$ for the same model. Right panel: UV surface brightness profile. Lines and symbols are the same as in the left panel. The horizontal dashed cyan line indicates the region below which systematic effects in the observational data by Momose et al. (2014) are important. The two shaded areas display the regions within the same $f_{\rm esc}^{\rm UV}$ ranges as for Lyα around the fiducial model.

(dark) and $0.1 \leqslant f_{\rm esc}^{\rm Ly\alpha} \leqslant 1.0$ (light). These ranges give an idea of the effect of a possible radial variation of the escape fraction due to the decrease of neutral gas with distance. The blue, green, and dotted red lines represent the power-law, NFW, and "bias-limited" models, respectively (for our fiducial choice $f_{\rm esc}^{\rm Ly\alpha} = 0.4$). The light blue dots represent the data and uncertainties from the observations by Momose et al. (2014) at $z = 3.1$, which are not reliable at $r > 40$ pkpc due to systematics (and therefore represented with open circles; Momose et al. 2014, see also Feldmeier et al. 2013). Magenta dots represent the data in the LAE overdensity bin $2.5 < \delta_{\rm LAE} < 5.5$ by Matsuda et al. (2012), which we also used in Mas-Ribas & Dijkstra (2016) given the value of our LAE overdensity.

Our fiducial model reproduces the observations well within the range $20 \lesssim r \lesssim 40$ pkpc. At shorter distances, the Lyα surface brightness may be enhanced by resonantly scattered Lyα that escapes from the central LAE and/or by fluorescence (Mas-Ribas & Dijkstra 2016). Systematics may in turn affect the data at $r \gtrsim 40$ pkpc, although the fiducial model reproduces the data from Matsuda et al. (2012) at these scales remarkably well. The other clustering prescriptions reproduce the observed surface brightness levels to within a factor of $\sim$2 at $20 \lesssim r \lesssim 40$ pkpc. In general, they give rise to flatter surface brightness profiles, which reflects that ξ_α is flatter at $r \lesssim 100$ pkpc in these models. The impact of the different clustering prescriptions becomes more severe at $r \lesssim 20$ pkpc. However, as we mentioned previously, here we expect the surface brightness profile to be enhanced by Lyα and LyC photons that escaped from the central LAE.

3.2. UV

The right panel in Figure 2 shows the predicted UV surface brightness profiles. We use the same symbols and colors as in the left panel. The horizontal dashed line shows the UV surface brightness level below which the data by Momose et al. (2014) is affected by systematics. This figure shows that at $20 \lesssim r \lesssim 40$ pkpc, our fiducial model predicts a UV profile above the observations by a factor of $\sim$3, while the other clustering prescriptions lie within a factor of $\sim$1.5–2. Our fiducial model thus results in an excess—by a factor of $\sim$3—of UV emission in the halos of LAEs. This result may reflect an overestimated star formation rate density in faint galaxies (i.e., $\rho_{\rm SFR}^{\rm sat}$). Based on analysis and modeling of *Hubble Space Telescope* observations aimed at detecting long-duration gamma-ray bursts host galaxies at high redshift, Trenti et al. (2012) inferred that $\sim$30% ($\sim$40%) of the total star formation at $z \sim 3$ ($z \lesssim 5$) occurs in galaxies too faint to be directly detected. This result is broadly consistent with the difference observed here, although the reduced emissivity value would also result in Lyα profiles below the observations by the same factor if no other parameters are tuned. An overestimated escape fraction $f_{\rm esc}^{\rm UV}$ would produce the same effect, though we consider this possibility unlikely. Alternatively, we may have overestimated the abundance of sources in the halo of LAEs due to clustering. We investigate the predicted luminosity and spatial distributions of satellites for various models and the dependence on LF parameter values in Appendix A. In Section 4.1, we further discuss the significant effect of a likely evolution of the Lyα rest-frame equivalent with the UV magnitude of the sources.

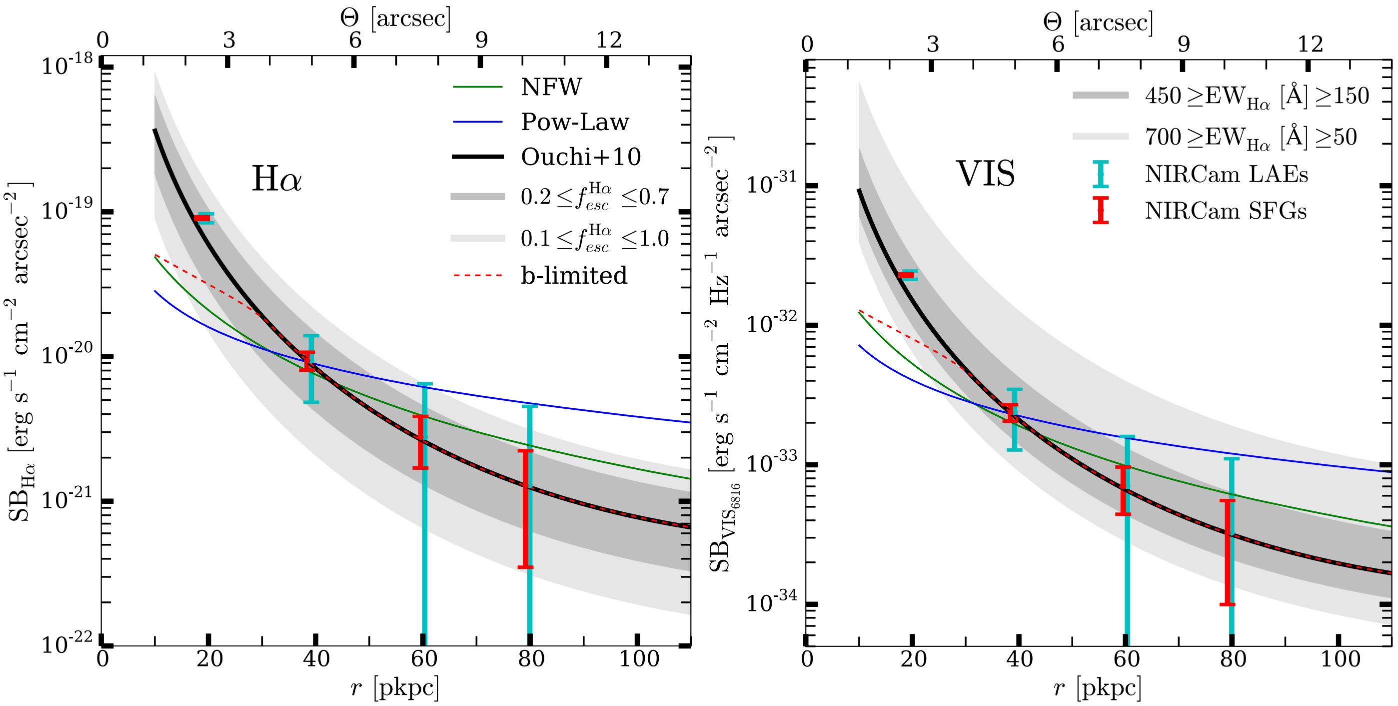

Figure 3. Left panel: radial Hα surface brightness profiles predicted by our different models. Lines and colors are the same as in Figure 2. The two shaded areas display the regions $0.2 \leqslant f_{\rm esc}^{\rm H\alpha} \leqslant 0.7$ and $0.1 \leqslant f_{\rm esc}^{\rm H\alpha} \leqslant 0.1$ for the fiducial model (black solid line). The blue (red) error bars indicate the values and uncertainties for the predicted observations of halos around LAEs (SFGs) described in Section 3.3.1 (Section 3.3.2). Right panel: same as in the left panel but considering the visible continuum emission at 6816 Å rest frame, computed assuming $\rm EW_{H\alpha} = 300$ Å. The shaded areas represent the ranges $450 \geqslant \rm EW_{H\alpha}$ [Å] $\geqslant 150$ and $700 \geqslant \rm EW_{H\alpha}$ [Å] $\geqslant 50$ for the fiducial model. The red and blue data points at $r = 20$ pkpc fall slightly above the solid black line due to averaging the signal around such a steep regions. The red vertical lines have been slightly shifted from their original position to facilitate the visualization.

3.3. Hα

Our predictions can be tested with future observations of Hα surface brightness profiles since Hα falls into the wavelength range covered by the *James Webb Space Telescope* (*JWST*; Gardner et al. 2006). In addition, Hα does not resonantly scatter, which simplifies interpreting its surface brightness profile compared to Lyα, and enables distinguishing between the different possible origins of LAHs.

The left panel in Figure 3 displays the predicted Hα surface brightness profiles. Our fiducial model is represented by the solid black line and (conservatively) assumes $f_{\rm esc}^{\rm H\alpha} = 0.4$. The impact of varying $f_{\rm esc}^{\rm H\alpha}$ and other models are shown in the same way as in Figure 2. The fiducial profile rises above 10^{-19} erg s^{-1} cm^{-2} arcsec^{-2} at distances $r \lesssim 20$ pkpc. The red and blue error bars represent the predicted uncertainties on the surface brightness profile, as if it was observed by the near-infrared camera (NIRCam) onboard *JWST* considering the two observational strategies described below. The surface brightness uncertainties are derived from the S/N, which decreases from S/N ~ 14 ($\sim$48) at $r = 20$ pkpc to S/N ~ 0.4 ($\sim$1.4) at $r = 80$ pkpc for halos around observed LAEs (star-forming galaxies, SFGs). We detail the calculations of the S/N in Appendix B. The left panel in Figure 3 indicates that the Hα emission predicted by the various models can be detected up to distances of $r \gtrsim 80$ pkpc when stacking the SFGs expected in the field of view (FOV).[9] Considering uniquely the emission around observed LAEs and our adopted observational strategy, NIRCam can prove the halos up to $r \sim 40$ pkpc, yielding upper limits at larger distances (see below). However, the presence of star formation at large distances from the central LAEs can be assessed up to $r \sim 80$ pkpc with observations of Hα and visible continuum radiation around star-forming galaxies (red error bars in both panels of Figure 3).

3.3.1. NIRCam Hα Observations of LAEs

The Multi-object Spectroscopy[10] observing mode of the near-infrared spectrograph (NIRSpec) would be desirable for our observations, given the large FOV, high spectral resolution (up to $R \sim 2700$), and the obtention of the spectra over a broad wavelength range. However, observations of nearby areas of the sky with contiguous (in the direction of dispersion) elements of the Micro-shutter Assembly result in spectra overlapping. The Integral-field Unit[11] (IFU) spectroscopy mode circumvents this problem with the use of three-dimensional spectral imaging data cubes but, in this case, the FOV is smaller than the expected halo of a single galaxy (FOV $\sim 3'' \times 3''$). Owing to the impracticability of the above modes, we consider the imaging capabilities of NIRCam for our calculations.

We adopt the narrowband (NB) filter F323N, with a bandpass of 0.038 μm, resulting in a resolution $R \sim 85$. We use this filter because it is the one closer to the Hα wavelength of interest, but we note that it is centered at a wavelength 3.2 μm, corresponding precisely to a Hα redshift $z = 3.9$. For this calculation, we assume the previous Hα flux and surface brightness at $z = 3.1$, but

---

[9] Zhang et al. (2016) already demonstrated in a recent work the strength of the stacking technic applied to Hα radiation around low redshift galaxies.

[10] https://jwst-docs.stsci.edu/display/JTI/NIRSpec+Multi+Object+Spectroscopy

[11] https://jwst-docs.stsci.edu/display/JTI/NIRSpec+IFU+Spectroscopy

Table 1
Lyα and UV Luminosity Function Parameters

	Lyα	UV$_{1500}$	Units
ϕ^*	0.92	1.56	(10^{-3} Mpc^{-3} $\log_{10} L^{-1}$/UV mag^{-1})
L^*/M^*[a]	5.8×10^{42}	-20.87	(erg s^{-1}/UV mag)
α	-1.50	-1.67	
$L_{\mathrm{Ly}\alpha}^{\mathrm{min}}/M_{\mathrm{UV}}^{\mathrm{min}}$[a]	10^{38}	-13	(erg s^{-1}/UV mag)
$L_{\mathrm{Ly}\alpha}^{\mathrm{max}}/M_{\mathrm{UV}}^{\mathrm{max}}$[a]	10^{44}	-24	(erg s^{-1}/UV mag)

Note.
[a] The parameters for Lyα are quoted in terms of luminosity and for UV$_{1500}$ in terms of UV magnitude.

Table 2
NIRCam Parameters

	Hα	VIS	Units
FOV	9.68	9.68	(arcmin^2)
A_{aper}	25	25	(m^2)
Filter	F323N	F335M	⋯
$\lambda_{\mathrm{obs}}(z = 3.9)$	3.237	3.362	(μm)
BW	0.038	0.352	(μm)
R	$\sim$85	$\sim$10	⋯
η	0.285	0.458	⋯
t_{exp}	10^4	10^4	(s)

we recalculate the sky background[12] at $z = 3.9$, obtaining $\mathrm{SB_{sky}}\,(3.20\ \mu\mathrm{m}) = 4 \times 10^{-20}$ erg s^{-1} cm^{-2} Å^{-1} arcsec^{-2}, consistent with the estimates by Giavalisco et al. 2002 for *HST* and the *Spitzer*/IRAC measurements by Krick et al. (2012). We set the observing time to 10^4 s.

We calculate the number of LAEs observable simultaneously in the FOV of NIRCam (FOV = $2 \times 2\rlap{.}'2 \times 2\rlap{.}'2$) as follows. We integrate the LAE LF at $z = 3.1$ by Ouchi et al. (2008) with the parameters in Table 1 for the luminosity range $10^{42} \leqslant L_{\mathrm{Ly}\alpha}$ (erg s^{-1}) $\leqslant 10^{44}$. This calculation yields a space density of LAEs $n_{\mathrm{LAE}} \sim 2 \times 10^{-3}$ cMpc^{-3}, in agreement with the findings by Ciardullo et al. (2006). The selected filter results in a redshift depth $\Delta z = 0.058$ centered at $z = 3.9$, giving rise to the simultaneous observation of $\sim$7 LAEs in the FOV.

Considering LAEs with luminosities $L_{\mathrm{LAE}} > 10^{42}$ erg s^{-1}, we can prove LAHs up to distances $\sim$40 pkpc, covering entirely the range of radii out to which the extended emission has been detected around LAEs. However, LAEs with these luminosities account for a small fraction of the total star-forming galaxy population. *JWST* surveys, as those already proposed by the NIRSpec and NIRCam GTO teams in the GOODS and CANDELS fields,[13] will detect a larger number of star-forming galaxies by means of the continuum and Hα radiation. We show below that stacking a larger sample of galaxies will enable proving extended Hα emission at larger distances from the center of galaxies and reaching low surface brightness levels, useful for assessing the role of cooling radiation.

3.3.2. NIRCam Hα Observations of SFGs

We predict the extended Hα emission around star-forming galaxies using the same observing configuration as above, but we estimate the number of SFGs as follows. We integrate the UV LF with the parameters by Kuhlen & Faucher-Giguère (2012) listed in Table 1 within the range $-24 \leqslant M_{\mathrm{UV}} \lesssim -17$, resulting in a space density $n_{\mathrm{SFG}} \sim 2 \times 10^{-2}$ cMpc^{-3}. The upper limit, $M_{\mathrm{UV}} \sim -17$, rises from considering $L_{\mathrm{UV}_{1500}}^{\mathrm{min}} \sim 0.025\, L_{\mathrm{UV}}^{*}$, and is consistent with the current limit of (unlensed) galaxy surveys (Finkelstein et al. 2015). The obtained space density results in the simultaneous observation of $\sim$86 SFGs in the FOV.

We refer the reader to Appendix B for a detailed description of the S/N calculations for the two above strategies.

3.4. VIS

The right panel in Figure 3 shows our predicted surface brightness profiles for the visible (VIS) continuum, with colors and labels as in the left panel. In this case, the shaded areas display the regions $450 \geqslant \mathrm{EW_{H\alpha}}$ [Å] $\geqslant 150$ and $700 \geqslant \mathrm{EW_{H\alpha}}$ [Å] $\geqslant 50$. *JWST* observations of the continuum radiation, in the visible wavelength range around $\sim$6800 Å rest frame, will enable proving star formation at large distances in the halos observing SFGs. Additionally, the VIS profiles will complement the UV profiles at large distances, allowing a better comparison of the different continua and line profiles which, in turn, unveils the contribution of the different processes yielding LAHs (see Section 4.2).

3.4.1. NIRCam VIS Observations of LAEs

We follow the previous observational strategies, using the S/N calculations presented in Appendix B and the instrumental parameters listed in Table 2.

We consider the same sample of LAEs as in Section 3.3.1 and the medium-band filter F335M, centered at 3.362 μm and with a bandpass 0.352 μm, resulting in a resolution $R \sim 10$. Since this filter is broader than that used to obtain the sample of LAEs, the observational depth will be larger, i.e., the number of galaxies falling into the filter band is larger than that of LAEs. This (undesired) additional number of galaxies may require the modeling of the sources and the removal of extra flux.

3.4.2. NIRCam VIS Observations of SFGs

For the observations of star-forming galaxies, we follow the same procedure and sample of galaxies as in Section 3.3.2. We use the same filter as above, F335M, noting that the same modeling of sources just discussed will also be necessary in this case.

4. Discussion

We discuss below the differences between the parameters for faint satellites and brighter galaxies and the dependence of our results on these values (Section 4.1). In Section 4.2, we show how the comparison between the Hα, Lyα, and continuum profiles breaks the degeneracies between the different mechanisms that give rise to the extended halos.

4.1. The EW-PDF(M_{UV}), Lyα Duty Cycle, and $C_{\mathrm{Ly}\alpha}$

For any fixed choice of satellite clustering, tuning the model to reproduce the observed Lyα surface brightness profile will cause it to overshoot the UV surface brightness profile (by a

---

[12] For the calculation of the background, we adopt Equation (22) in the NIRSpec technical note http://www.stsci.edu/~tumlinso/nrs_sens_2852.pdf.

[13] https://confluence.stsci.edu/display/STUCP/JWST+Guaranteed+Time+Observers+Cycle+1+Plans

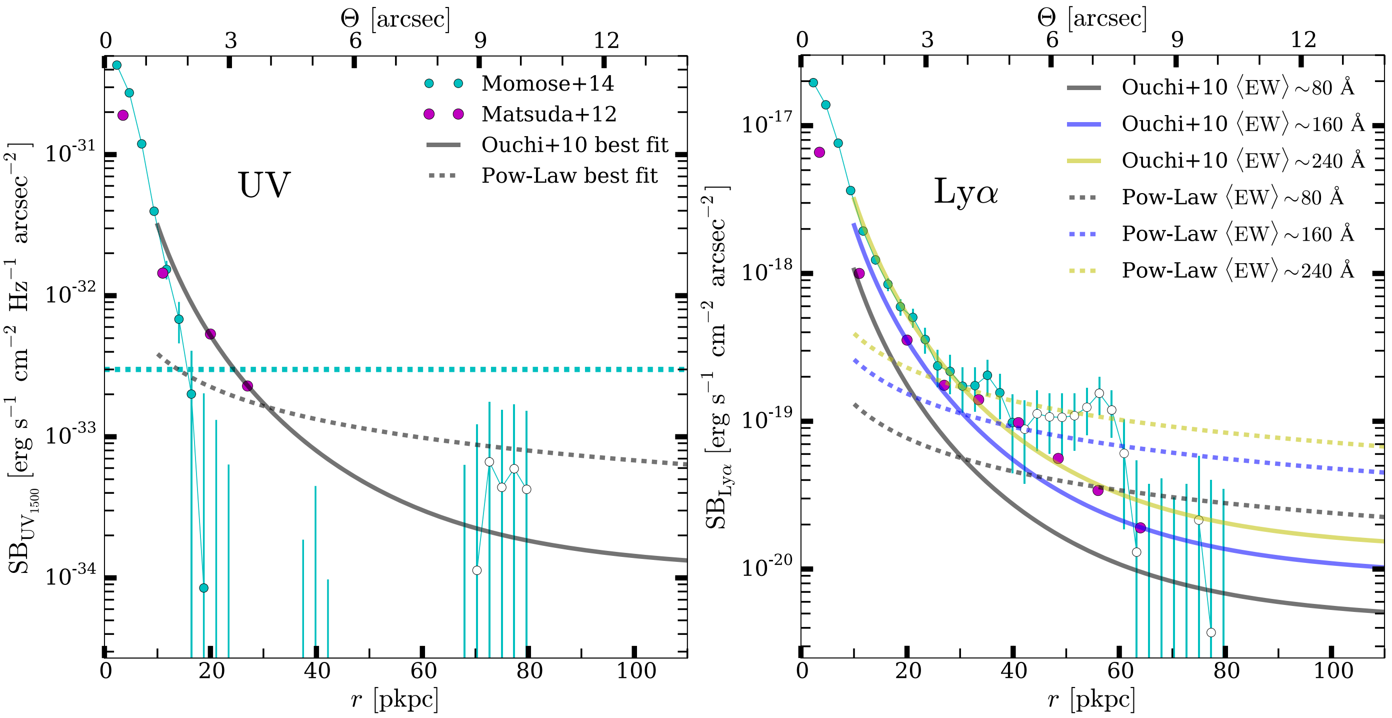

Figure 4. Left panel: radial UV surface brightness profiles with physical distance from the central galaxy for the fiducial (solid gray line) and the power-law (dashed line) models, reduced by a factor of three and two, respectively, to better fit the data. Magenta and cyan dots, line, and bars denote the data as in Figure 2. Right panel: predicted Lyα surface brightness profiles for the two models in the left panel assuming different population-averaged Lyα EW (rest frame). The profiles with $\langle \mathrm{EW} \rangle \sim 80$ Å correspond to the "best-fit" profiles in the left panel assuming the same escape fraction for Lyα and UV.

factor of up to ~1.5–3, depending on the clustering model, see Figure 2). This effect can be easily remedied by requiring that $f_{\mathrm{esc}}^{\mathrm{Ly}\alpha} > f_{\mathrm{esc}}^{\mathrm{UV}}$. However, resonant scattering typically enlarges the total path that Lyα photons travel through dusty multiphase media, which increases the probability that these photons are destroyed by dust grains, relative to that of the continuum (see, e.g., Laursen et al. 2013; Gronke & Dijkstra 2014). We therefore consider that it is not reasonable to require that $f_{\mathrm{esc}}^{\mathrm{Ly}\alpha} > f_{\mathrm{esc}}^{\mathrm{UV}}$ for the *entire population*.

It is more likely that our adopted conversion factors from star formation rate density to integrated volume emissivity (C_x in Equation (6)) differ somewhat. Our current choices for $C_{\mathrm{Ly}\alpha}$ and C_{UV} imply that *all* star-forming galaxies produce a Lyα line with a rest-frame equivalent width of EW ~ 80 Å (see, e.g., Dijkstra & Westra 2010), but the EW of the Lyα line can be larger by a factor of a few for very young stellar populations (e.g., Schaerer 2003). C_x, especially $C_{\mathrm{Ly}\alpha}$, can be increased for lower metallicities, low SFR galaxies, and/or for more top-heavy IMFs (Raiter et al. 2010; Forero-Romero & Dijkstra 2013; Mas-Ribas et al. 2016, see also the review by Kennicutt & Evans 2012 for Hα and UV). This interpretation is supported by the short duty cycle of Lyα-selected LAEs reported by Ouchi et al. (2010), which illustrates that the larger EW objects are dominated by young stellar populations.

Our results suggest that, in order to simultaneously reproduce the observed Lyα and UV surface brightness profiles, we need the *population-averaged* rest-frame EW to be ~1.5–3 larger, i.e., we need $\langle \mathrm{EW} \rangle \sim 120$–240 Å for Ly$\alpha$. "Population averaged" here refers to an average over all satellite galaxies with $M_{\mathrm{UV}} \gtrsim -17$. In the left panel of Figure 4, we reduced the UV surface brightness profiles of the fiducial and power-law models by a factor of three and two, respectively, to obtain a good fit to the data. In the right panel of the same figure, we present the corresponding Lyα profiles for different values of $\langle \mathrm{EW} \rangle$. The dashed and solid black lines denote the power-law and fiducial profiles, respectively, when considering the same escape fraction for Lyα and UV, as in our previous calculations, i.e., $\langle \mathrm{EW} \rangle \sim 80$ Å. In this case, the profiles fall below the observations as expected. Considering $\langle \mathrm{EW} \rangle \sim 160$ Å, the fiducial model (*s*olid blue line) reproduces the data by Matsuda et al. (2012) well for $r \lesssim 30$ pkpc, but is slightly lower at larger distances. Accounting for the contribution of the central galaxy, the power-law model (dashed blue line) may match the data at $r \lesssim 40$ pkpc, although it is above the observations by Matsuda et al. (2012) at larger distances. If we consider $\langle \mathrm{EW} \rangle \sim 240$ Å (dashed and solid yellow lines), the models matches the data well at any distance, but if the central galaxy is added, they may overpredict the profiles. Therefore, we conclude from this calculation that an average equivalent width around $\langle \mathrm{EW} \rangle \sim 160$ Å may provide a reasonable fit to the data, although the exact value depends on the specific model and contribution of the central galaxy.

Is this $\langle \mathrm{EW} \rangle$ requirement reasonable? There is strong observational support that the Lyα EW-PDF evolves toward fainter UV luminosities. Dijkstra & Wyithe (2012) presented a fitting formula for $P(\mathrm{EW}|M_{\mathrm{UV}}, z)$ constrained by observations. The solid black line in Figure 5 displays $\langle \mathrm{EW} \rangle$ (rest frame) as a function of M_{UV} as given by this fitting formula (see Schenker et al. 2014 for an alternative parameterization). Figure 5 shows that for bright LBGs ($M_{\mathrm{UV}} \lesssim -22$, see Figures A1–A3 of Dijkstra & Wyithe 2012, which is based in data by Shapley et al. 2003), $\langle \mathrm{EW} \rangle \sim 0$. However, $\langle \mathrm{EW} \rangle$ rapidly rises toward lower UV luminosities (based on data by Stark et al. 2010) and reaches $\langle \mathrm{EW} \rangle \sim 55$ Å at $M_{\mathrm{UV}} \sim -19$. Due to the lack of observational data, Dijkstra & Wyithe (2012) adopted

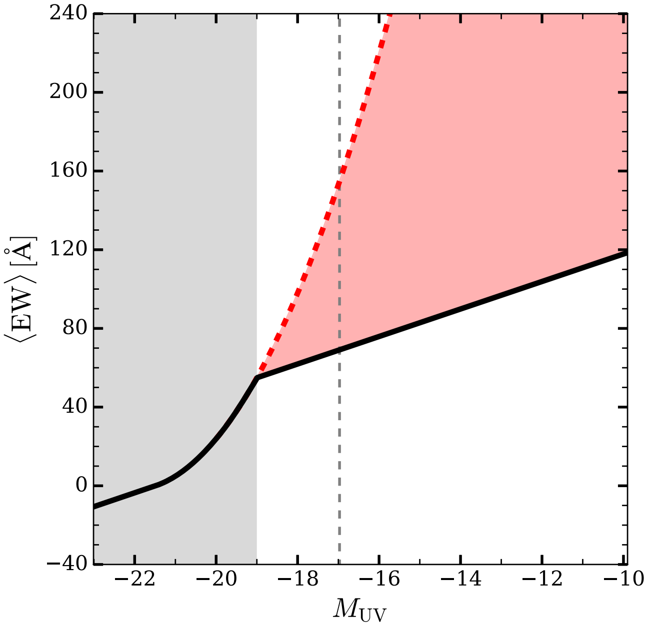

Figure 5. Mean Lyα rest-frame equivalent width, ⟨EW⟩, as a function of $M_{\rm UV}$, parameterized following the fitting formula by Dijkstra & Wyithe (2012; solid black line), and extrapolating the evolution observed by Stark et al. (2010) within the range $-19 \gtrsim M_{\rm UV} \gtrsim -22$ (dashed red line). The red and the gray shaded areas represent the regions between the two evolutions and where the model is constrained by observations, respectively, and the dashed vertical line denotes the current observational limit, $M_{\rm UV} = -17$, corresponding to $\langle {\rm EW}\rangle = 69$ Å. This figure shows that the modest extrapolation of the observed evolution of ⟨EW⟩ with $M_{\rm UV}$ by Dijkstra & Wyithe (2012) can partially account for simultaneously reproducing the observed surface brightness profiles of UV and Lyα halos, while steeper evolutions are required for a complete match.

(conservatively) the same slope as in the range $M_{\rm UV} \leqslant -21.5$ for the region $M_{\rm UV} \geqslant -19$ for the evolution of equivalent width. This modest extrapolation can partially account for simultaneously matching the UV and Lyα surface brightness profiles. However, the evolution may be steeper than assumed by these authors (see, e.g., the recent work at $z = 7$ by Ota et al. 2017). The dashed red line in Figure 5 extrapolates the evolution observed by Stark et al. (2010) in the range $-19 \gtrsim M_{\rm UV} \gtrsim -22$, reaching the required value to match both profiles, $\langle {\rm EW}\rangle = 240$, quickly after $M_{\rm UV} \sim -16$. The shaded red region shows the area between these two evolutions.

4.2. Comparing Hα, Lyα, and Continuum Profiles

Joint analyses of Hα, Lyα, and continuum surface brightness profiles are very useful because they enable disentangling the possible origins of the extended emission. The differences will rise from the physical mechanisms that can yield photons of these three wavelength bands. (i) Continuum radiation is a direct tracer of star formation because it is only produced in the ISM and it is not a resonant transition. (ii) Hα is also produced in the ISM via recombinations following hydrogen ionization but additionally can be produced far from the star-forming regions if ionizing photons reach those distances and ionize the more distant gas (fluorescence). (iii) Lyα can be produced via the two previous mechanisms, but also by the collisional excitation of neutral hydrogen accreted into the central galaxy (gravitational cooling). Additionally, Lyα is a resonant transition that allows the Lyα photons to scatter away from the sites where they are produced. The flow chart and plots of Figure 6 represent a simple method to identify the mechanisms playing a role in the extended emission. The idealized diffuse halo in the left part of the figure shows extended Lyα (in blue) but compact Hα and continuum emission (in red and green, respectively). This scenario is a clear indication of scattering and/or cooling, as we describe below. The middle plot illustrates a more extended Hα halo compared to that of the continuum, indicating that fluorescence is important. When star formation occurs far from the center, the continuum will also appear more extended, as schematically illustrated in the right plot. Hα and Lyα halos will also be extended in this case accounting for the nebular radiation of the satellite sources and can be subject to the extra contribution of fluorescence, scattering, and/or cooling. Additional information can be obtained from the radial profiles as follows.

1. A strong suppression of the continuum and Hα surface brightness compared to our predictions at a fixed Lyα surface brightness favors the scattering and cooling models. Models that purely invoke scattering to explain spatially extended Lyα halos cannot produce extended continuum and Hα halos. Cooling gives rise to Hα and UV halos that are suppressed by a factor of ∼10 compared to our predictions here (see Dijkstra 2014 for a review discussing the Hα and UV continuum signatures of cooling radiation). This scenario corresponds to the 2D plot on the left part of Figure 6, where Lyα emission appears more extended than the Hα and continuum.
2. Comparing Hα and Lyα surface brightness profiles constrains to what extent scattering affects the Lyα surface brightness profile. This is because the volume emissivity of Lyα and Hα closely track each other, while only Lyα photons undergo resonant scattering. Scattering systematically flattens the Lyα surface brightness profile, as the Lyα photons diffuse outwards prior to escape.
3. Comparing Hα and continuum surface brightness profiles can determine the importance of nebular against fluorescent emission: if no ionizing photons escape from either the central LAE or the satellites, then the Hα is produced in dense nebulae surrounding O and B stars and we expect the continuum and Hα volume emissivity to closely track each other (co-spatial green and red regions in the left plot of Figure 6). Instead, if ionizing photons escape efficiently from low-luminosity galaxies (as expected theoretically and observationally; e.g., Wise et al. 2014; Japelj et al. 2017, see also Dijkstra et al. 2016 and references therein), then we expect gas in the CGM to fluoresce in response to the enhanced local ionizing radiation field (see Mas-Ribas & Dijkstra 2016). In this case, each satellite galaxy is more extended in Hα than in the continuum. The resulting overall Hα surface brightness profile should also be more extended (middle plot in Figure 6 where the red region presents a larger area than the green one).

5. Conclusions

We have quantified the contribution of faint (satellite) galaxies ($M_{\rm UV} > -17$) to spatially extended Lyα and UV halos around star-forming galaxies. We have applied the analytic formalism developed in Mas-Ribas & Dijkstra (2016) to model the halos around LAEs at $z = 3.1$ for several different satellite clustering prescriptions. The predicted surface brightness depends linearly on the product $\bar{\epsilon}_x^{\rm sat} f_{\rm esc}^x\, b_x$, where x refers

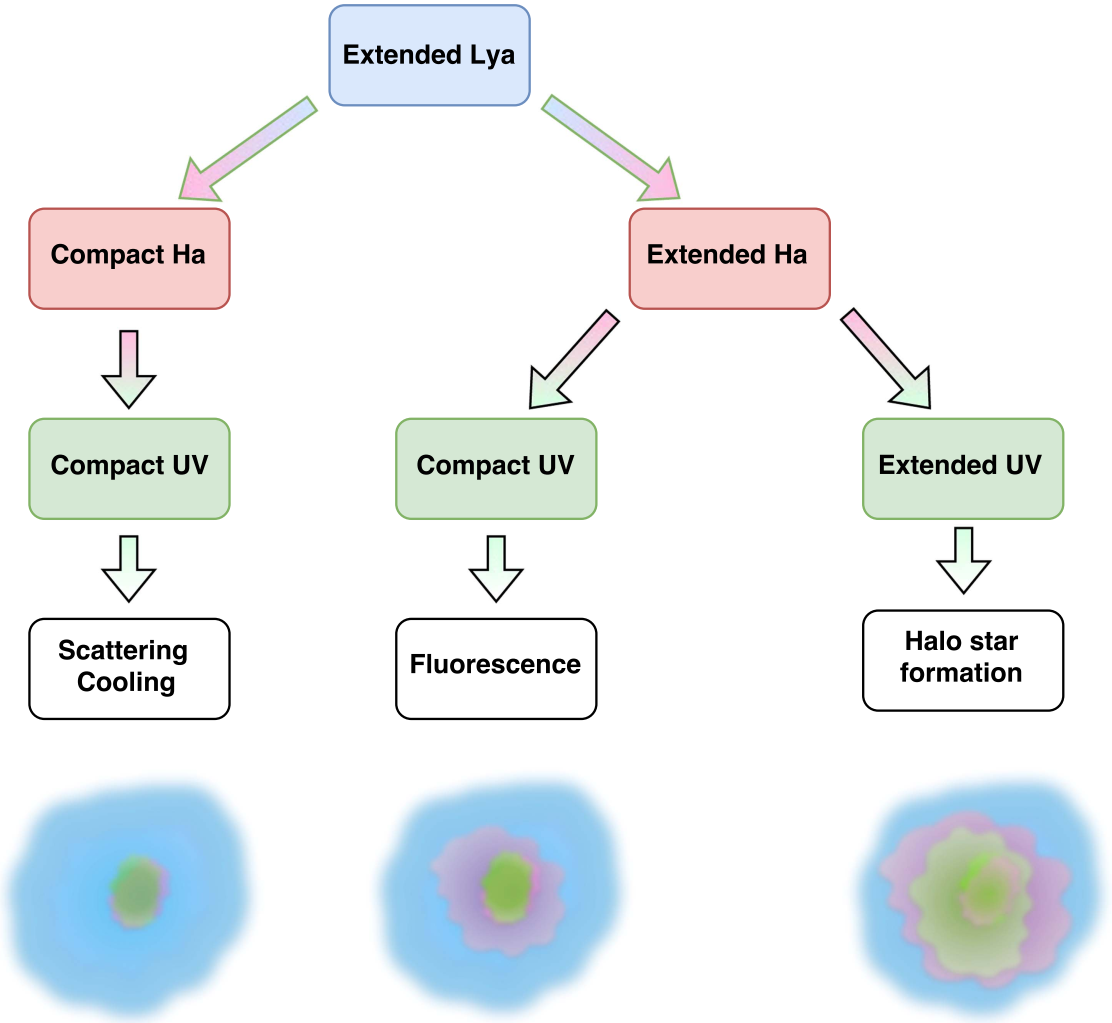

Figure 6. Flow chart and plots representing the effect of the different radiative processes on the diffuse extended halos. The left plot displays extended Lyα emission only in blue, indicative of significant scattering and/or cooling effects. The middle plot shows a larger extent for the Hα emission than that of the continuum (red and green, respectively), implying a contribution of fluorescence. The right plot shows extended emission for all cases, indicating the presence of star formation beyond the central galaxy.

to UV, Hα, and Lyα. Here, $\bar{\epsilon}_x^{\rm sat}$ denotes the integrated emissivity of faint galaxies, which is directly linked to the star formation rate density in these galaxies (see Section 2.1), b_x denotes the emission bias (see Section 2.2.2), and $f_{\rm esc}^x$ denotes the escape fraction (see Section 2.3). Our main results are as follows.

1. All of our models give rise to spatially extended Lyα and UV halos at a level that is broadly consistent with observations at $20 \lesssim r \lesssim 40$ pkpc from the centers of LAEs, for a reasonable choice of the product $\bar{\epsilon}_x^{\rm sat} f_{\rm esc}^x\, b_x$. The flatness of the surface brightness profiles depends on the clustering prescription at small scales ($r \lesssim 100$ pkpc). This result supports the notion that faint satellite sources can explain the extended emission and constrain their presence in the halo of more massive galaxies.
2. For any fixed choice of satellite clustering, the ratio between predicted and observed surface brightness at $20 \lesssim r \lesssim 40$ pkpc is higher for UV than for Lyα. In other words, any given model that we tune to perfectly reproduce the observed Lyα surface brightness profile will overshoot the predicted UV surface brightness profile (by a factor of up to $\sim$3, depending on the clustering model). We discussed in Section 4.1 that this implies that we need the average Lyα EW (rest frame) of satellite galaxies to lie around $\langle {\rm EW}\rangle \sim 120$–240 Å, the lower end of which is consistent with the observed evolution of the Lyα EW-PDF as a function of $M_{\rm UV}$ (see Figure 5 and Dijkstra & Wyithe 2012). We found that extrapolating the observed evolution of EW with $M_{\rm UV}$ can at least partially accommodate these differences.
3. Because there exist multiple alternative explanations for the presence of extended Lyα halos around star-forming galaxies (including scattering, cooling, fluorescence, etc.; see Section 1), it is important to investigate whether there are observables that distinguish between different mechanisms. We have therefore also predicted Hα surface brightness profiles. Our calculations demonstrate that *JWST* will be able to probe Hα surface brightness profiles out to distances $r \gtrsim 80$ pkpc and at levels down to ${\rm SB}_{{\rm H}\alpha} \sim 10^{-21}$ erg s^{-1} cm^{-2} arcsec^{-2}. These Hα observations will enable breaking the degeneracies between the different mechanisms that give rise to extended halos.

We generally expect a progressive steepening of the surface brightness profiles from Lyα to Hα to continuum. The exact quantitative steepening depends on how efficiently ionizing photons escape from the central galaxy and its surrounding satellites, and also the distribution of self-shielding gas in the CGM of the central galaxy and in the central parts of the satellite sources. These more detailed calculations are beyond the scope of our current work. Observations of extended halos complement other recently proposed ways to constraint escape fractions, such as using Hβ EWs (Zackrisson et al. 2013, 2017), Lyα line profiles (Verhamme et al. 2015, 2017; Dijkstra et al. 2016), and covering factor values (Jones et al. 2012, 2013; Leethochawalit et al. 2016; Reddy et al. 2016). We will apply our method to investigate the average ionizing escape fraction of galaxies during the epoch of cosmic reionization in an upcoming work. We also plan to further constrain our modeling by including predictions for the spatial distribution (radial offset) of long-duration GRBs from the center of the dark matter host halo, which will depend on the star formation rate and metallicity of the faint satellites (Trenti et al. 2015). Current success rates for the detection of GRB host galaxies at $z \sim 3$–5 are $\sim$60% (Greiner et al. 2015), thus it might be possible that a fraction of the "hostless" GRBs inhabits and probes faint (undetected) satellite sources.

Our results have focused on using a LAE as the central galaxy. The reason for using LAEs is that there exists good observational data for Lyα halos. However, as Lyα halos appear ubiquitously around star-forming galaxies (Steidel et al. 2011; Wisotzki et al. 2016), our analysis can be applied to different populations, allowing for a better understanding on the physical processes governing galaxy formation and evolution, and the role played by faint, undetected sources to the cosmic photon budget at different epochs.

L.M.R. is grateful to the ENIGMA group at the MPIA in Heidelberg for kind hospitality and inspiring discussions. We thank the anonymous referee for a prompt report and careful reading that improved the clarity of our work. Thanks to Joop Schaye and Zoltán Haiman for comments on the likely distance dependence of the escape fraction, and Nobunari Kashikawa for pointing clustering aspects. We thank Joel Primack, David Sobral, Kyoung-Soo Lee, Lutz Wisotzki, Hakon Dahle, Ainar Drews, Marcia and George Rieke, Benjamin Racine, Dan Stark, Johan Fynbo, Eros Vanzella, Jorryt Matthee, and Michal Michalowski for their comments and suggestions. M.D. is grateful to the Astronomy Department in UCSB for kind hospitality.

Appendix A
Distribution of Satellite Sources

We calculate the number of sources in concentric shells at a distance r around the central galaxy for our fiducial clustering model using the expression

$$n(r) = (1+z)^3 \int_{r_{\min}}^{r_{\max}} 4\pi r^2 \,[1+\xi(r)]\, dr \int_{L_{\min}}^{L_{\max}} \phi(L)\, dL, \tag{10}$$

where $r_{\min}$, $r_{\max}$ and $L_{\min}$, $L_{\max}$ denote the radial limits of the shell and luminosity limits, respectively, and $\phi(L)dL$ is the Schechter LF (Schechter 1976)

$$\phi(L)dL = \phi^*(L/L^*)^{\alpha} \exp(L/L^*)\, d(L/L^*). \tag{11}$$

We run the Poisson distribution on the obtained $n(r)$ values to randomly draw a distribution of 10,000 integer numbers of galaxies at every concentric shell. The parameters of the LFs are quoted in Table 1 and are taken from the fitting formula by Kuhlen & Faucher-Giguère (2012) for UV, and from Ouchi et al. (2008) for Lyα.[14]

Figure 7 displays the distribution of sources in the range $10 \leqslant r \leqslant 160$ pkpc, covering the entire region of interest, using the parameters in Table 1. The left panel represents the distribution of Lyα luminosities and the right one of UV magnitudes. Every panel quotes the average number of galaxies from Equation (10), $n(r)$. Our fiducial model predicts $\sim$1–2 sources in the range $L_{Ly\alpha} \sim 10^{40}$–$10^{41}$ erg s^{-1}, the number increasing for fainter luminosities. For UV, we obtain $\sim$1 ($\sim$2) sources with magnitudes $M_{\rm UV} \sim -17(-16)$. We have also computed the distribution of galaxies at different radial distances (not shown); the number of galaxies decreases considerably outwards from the center, as expected given the profile of the correlation function, and the luminosity and magnitude distributions display similar profiles than those in Figure 7.

We obtain different emissivity values when integrating the LFs compared to those computed previously from the star formation rate density (a factor $\sim$4.6 reduction for Lyα, and $\sim$1.78 increase for UV). These differences may be interpreted as corrections to the adopted values for any of the parameters $\bar{\epsilon}_x$, $f^x_{\rm esc}$, and/or b_x, but changes in the expressions relating emissivity and star formation may (partially or totally) also accommodate such differences, since they depend on the adopted IMF and other parameters (Hopkins & Beacom 2006). In addition, we assess below the effect introduced by varying parameters of the LFs. Setting a minimum Lyα luminosity of $L_{\rm Ly\alpha} = 10^{34}$ erg s^{-1} and an extreme minimum UV magnitude $M_{\rm UV} \sim -3$ results in emissivity changes by less than 1% (10%) for Lyα (UV) functions compared to the previous case. We obtain, however, thousands of sources in the halo. With lower limits set to $L_{\rm Ly\alpha} = 10^{41}$ erg s^{-1} and $M_{\rm UV} \sim -17$, the increase of UV emissivity is now lower, a factor of $\sim$1.35, and Lyα is lower by a factor of $\sim$5.45. The total average number of sources is $\sim$3 ($\sim$1) for UV (Lyα), all with luminosities corresponding to the lower limits. As mentioned above, several works indicate a steeper Lyα faint-end slope than the ones in Table 1 (Gronke et al. 2015; Sobral et al. 2017). Considering $\alpha = -1.8$ for both functions, the UV emissivity is now above by a factor of $\sim$2.5 and Lyα below by a factor of $\sim$2 when compared to the emissivity from star formation. This result demonstrates that the values for the emissivity are more sensible to changes of the faint-end slope than in the lower limits of the LFs.

Appendix B
NIRCam Signal-to-noise Calculation

We calculate the S/N in our observations as $\mathrm{S/N} = N_s/\sqrt{N_s + N_{\rm sky}}$. We ignore the instrumental noise and systematics since these depend on the observational methodology, i.e.,

---

[14] For comparison, we use the two LFs because, although the parameters of the UV and Lyα LFs are related, this relation depends on several assumptions and is not entirely understood (see, e.g., Figure 4 in Garel et al. 2015).

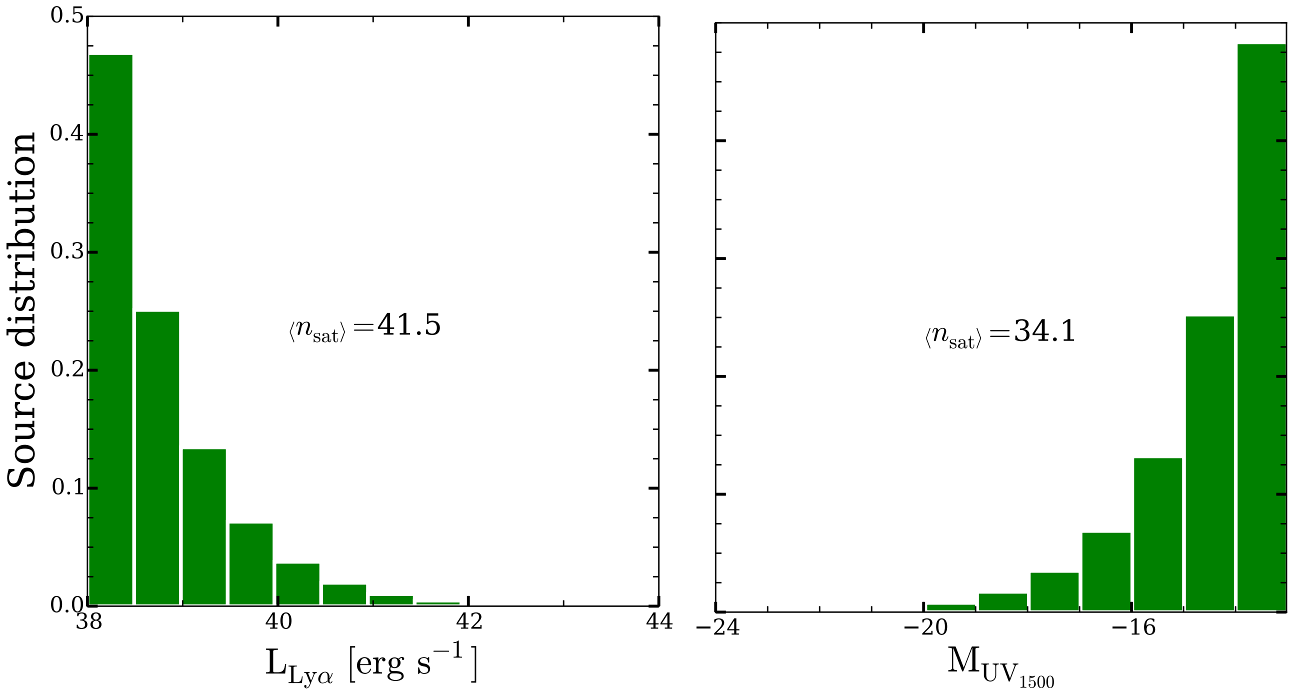

Figure 7. Distribution of luminosities for satellite sources in the range $10 \leqslant r \leqslant 160$ pkpc from the central LAE, using the parameters in Table 1 and our fiducial clustering model. The left panel represents the distribution of Lyα luminosities and the right panel those of UV magnitudes. Every panel quotes the average number of galaxies obtained from Equation (10). Both panels indicate the presence of a few sources close to the observational thresholds, and a larger number of significantly fainter objects.

number of exposures, number of pixels for source and background calculations, rms fluctuations in the detector response after flat-fielding, or the use or not of auxiliary calibration data for the dark-current subtraction. Given the large FOV, we expect our noise to be dominated by photons instead of systematics. Some of the systematics are accounted for in the system throughput parameter η and, in any case, we check our results with the online calculator tool (see below). N_s and $N_{\rm sky}$ are the azimuthally averaged photon counts for the sources and sky, respectively, and are computed as

$$N_s = \frac{f_{\rm H\alpha}}{h\,\nu_{\rm H\alpha}^{\rm obs}} A_{\rm aper}\,\eta\,t_{\rm exp}, \tag{12}$$

$$N_{\rm sky} = \frac{f_{\rm sky}}{h\,\nu_{\rm H\alpha}^{\rm obs}} {\rm BW}\,A_{\rm aper}\,\eta\,t_{\rm exp}. \tag{13}$$

Here, $f_{\rm H\alpha}$ and $f_{\rm sky}$ are the Hα and sky fluxes, obtained integrating the surface brightness over the area of the corresponding distance bin (annulus) around the central galaxy. $h\nu_{\rm H\alpha}^{\rm obs}$ denotes the Hα photon energy at $z = 3.9$, $A_{\rm aper}$ is the aperture of *JWST*, η represents the "efficiency" (total system throughput), and $t_{\rm exp}$ is the total exposure time. In the sky background calculation, we multiply by the filter bandpass (BW) since the sky is in units of flux density. This is also the case for the calculation of the VIS continuum. Table 2 lists the values adopted for the above parameters.

We have used the online *JWST* Exposure Time Calculator[15] (ETC) and have found that the results are consistent with our calculations. We find that a line flux of $f_{\rm H\alpha} \sim 5 \times 10^{-19}$ erg s^{-1} cm^{-2} and $t_{\rm exp} \sim 10^4$ s corresponds to 1σ (S/N = 1), although this flux can vary by a factor of a few when accounting for different readout modes (see, e.g., http://www.stsci.edu/jwst/instruments/nircam/docarchive/JWST-STScI-001721.pdf).

References

Alavi, A., Siana, B., Richard, J., et al. 2014, ApJ, 780, 143
Alavi, A., Siana, B., Richard, J., et al. 2016, ApJ, 832, 56
Bacon, R., Vernet, J., Borisova, E., et al. 2014, Msngr, 157, 13
Bahcall, J. N., & Spitzer, L., Jr. 1969, ApJL, 156, L63
Barnes, L. A., Garel, T., & Kacprzak, G. G. 2014, PASP, 126, 969
Bielby, R. M., Tummuangpak, P., Shanks, T., et al. 2016, MNRAS, 456, 4061
Blanc, G. A., Adams, J. J., Gebhardt, K., et al. 2011, ApJ, 736, 31
Bouwens, R. J., Illingworth, G. D., Oesch, P. A., et al. 2015, ApJ, 803, 34
Brocklehurst, M. 1971, MNRAS, 153, 471
Bryan, G. L., & Norman, M. L. 1998, ApJ, 495, 80
Calzetti, D., Armus, L., Bohlin, R. C., et al. 2000, ApJ, 533, 682
Calzetti, D., Kinney, A. L., & Storchi-Bergmann, T. 1994, ApJ, 429, 582
Cantalupo, S., Lilly, S. J., & Haehnelt, M. G. 2012, MNRAS, 425, 1992
Carilli, C. L. 2011, ApJL, 730, L30
Chang, T.-C., Pen, U.-L., Bandura, K., & Peterson, J. B. 2010, Natur, 466, 463
Ciardullo, R., Gronwall, C., Hickey, T., et al. 2006, BAAS, 38, 1146
Croft, R. A. C., Miralda-Escudé, J., Zheng, Z., et al. 2016, MNRAS, 457, 3541
Dawson, K. S., Schlegel, D. J., Ahn, C. P., et al. 2013, AJ, 145, 10
Dekel, A., & Birnboim, Y. 2006, MNRAS, 368, 2
Dijkstra, M. 2014, PASA, 31, 40
Dijkstra, M., Gronke, M., & Venkatesan, A. 2016, ApJ, 828, 71
Dijkstra, M., & Jeeson-Daniel, A. 2013, MNRAS, 435, 3333
Dijkstra, M., & Kramer, R. 2012, MNRAS, 424, 1672
Dijkstra, M., & Loeb, A. 2009, MNRAS, 400, 1109
Dijkstra, M., & Westra, E. 2010, MNRAS, 401, 2343
Dijkstra, M., & Wyithe, J. S. B. 2012, MNRAS, 419, 3181
Doré, O., Bock, J., Ashby, M., et al. 2014, arXiv:1412.4872
Drake, A. B., Guiderdoni, B., Blaizot, J., et al. 2016, arXiv:1609.02920
Eisenstein, D. J., Weinberg, D. H., Agol, E., et al. 2011, AJ, 142, 72
Fardal, M. A., Katz, N., Gardner, J. P., et al. 2001, ApJ, 562, 605
Faucher-Giguère, C.-A., Kereš, D., Dijkstra, M., Hernquist, L., & Zaldarriaga, M. 2010, ApJ, 725, 633
Feldmeier, J. J., Hagen, A., Ciardullo, R., et al. 2013, ApJ, 776, 75

---

[15] https://jwst.etc.stsci.edu/

Finkelstein, S. L., Ryan, R. E., Jr., Papovich, C., et al. 2015, ApJ, 810, 71
Forero-Romero, J. E., & Dijkstra, M. 2013, MNRAS, 428, 2163
Fynbo, J. U., Møller, P., & Thomsen, B. 2001, A&A, 374, 443
Fynbo, J. U., Møller, P., & Warren, S. J. 1999, MNRAS, 305, 849
Gardner, J. P., Mather, J. C., Clampin, M., et al. 2006, SSRv, 123, 485
Garel, T., Blaizot, J., Guiderdoni, B., et al. 2015, MNRAS, 450, 1279
Garel, T., Guiderdoni, B., & Blaizot, J. 2016, MNRAS, 455, 3436
Gawiser, E., Francke, H., Lai, K., et al. 2007, ApJ, 671, 278
Giavalisco, M., Sahu, K., & Bohlin, R. C. 2002, New Estimates of the Sky Background for the HST Exposure Time Calculator. Sci. Rep. ACS. (Baltimore, MD: STScI)
Gong, Y., Cooray, A., Silva, M. B., Santos, M. G., & Lubin, P. 2011, ApJL, 728, L46
Gordon, K. D., Clayton, G. C., Misselt, K. A., Landolt, A. U., & Wolff, M. J. 2003, ApJ, 594, 279
Greiner, J., Fox, D. B., Schady, P., et al. 2015, ApJ, 809, 76
Gronke, M., & Dijkstra, M. 2014, MNRAS, 444, 1095
Gronke, M., Dijkstra, M., Trenti, M., & Wyithe, S. 2015, MNRAS, 449, 1284
Guaita, L., Gawiser, E., Padilla, N., et al. 2010, ApJ, 714, 255
Haiman, Z., Spaans, M., & Quataert, E. 2000, ApJL, 537, L5
Hayes, M., Schaerer, D., Östlin, G., et al. 2011, ApJ, 730, 8
Hopkins, A. M., & Beacom, J. F. 2006, ApJ, 651, 142
Japelj, J., Vanzella, E., Fontanot, F., et al. 2017, MNRAS, 468, 389
Jones, T., Stark, D. P., & Ellis, R. S. 2012, ApJ, 751, 51
Jones, T. A., Ellis, R. S., Schenker, M. A., & Stark, D. P. 2013, ApJ, 779, 52
Kennicutt, R. C., Jr. 1998, ARA&A, 36, 189
Kennicutt, R. C., & Evans, N. J. 2012, ARA&A, 50, 531
Kereš, D., Katz, N., Weinberg, D. H., & Davé, R. 2005, MNRAS, 363, 2
Khaire, V., & Srianand, R. 2015, ApJ, 805, 33
Konno, A., Ouchi, M., Nakajima, K., et al. 2016, ApJ, 823, 20
Kovač, K., Somerville, R. S., Rhoads, J. E., Malhotra, S., & Wang, J. 2007, ApJ, 668, 15
Krick, J. E., Glaccum, W. J., Carey, S. J., et al. 2012, ApJ, 754, 53
Kuhlen, M., & Faucher-Giguère, C.-A. 2012, MNRAS, 423, 862
Lake, E., Zheng, Z., Cen, R., et al. 2015, arXiv:1502.01349
Lapi, A., Mancuso, C., Celotti, A., & Danese, L. 2017, ApJ, 835, 37
Laursen, P., Duval, F., & Östlin, G. 2013, ApJ, 766, 124
Laursen, P., Razoumov, A. O., & Sommer-Larsen, J. 2009, ApJ, 696, 853
Laursen, P., & Sommer-Larsen, J. 2007, ApJL, 657, L69
Leethochawalit, N., Jones, T. A., Ellis, R. S., Stark, D. P., & Zitrin, A. 2016, ApJ, 831, 152
Lewis, A., Challinor, A., & Lasenby, A. 2000, ApJ, 538, 473
Li, T. Y., Wechsler, R. H., Devaraj, K., & Church, S. E. 2016, ApJ, 817, 169
Livermore, R. C., Finkelstein, S. L., & Lotz, J. M. 2017, ApJ, 835, 113
Madau, P., Pozzetti, L., & Dickinson, M. 1998, ApJ, 498, 106
Maiolino, R., Russell, H. R., Fabian, A. C., et al. 2017, Natur, 544, 202
Mármol-Queraltó, E., McLure, R. J., Cullen, F., et al. 2016, MNRAS, 460, 3587
Mas-Ribas, L., & Dijkstra, M. 2016, ApJ, 822, 84
Mas-Ribas, L., Dijkstra, M., & Forero-Romero, J. E. 2016, ApJ, 833, 65
Matsuda, Y., Yamada, T., Hayashino, T., et al. 2012, MNRAS, 425, 878
Møller, P., & Warren, S. J. 1998, MNRAS, 299, 661
Momose, R., Ouchi, M., Nakajima, K., et al. 2014, MNRAS, 442, 110
Momose, R., Ouchi, M., Nakajima, K., et al. 2016, MNRAS, 457, 2318
Navarro, J. F., Frenk, C. S., & White, S. D. M. 1997, ApJ, 490, 493
Nestor, D. B., Shapley, A. E., Kornei, K. A., Steidel, C. C., & Siana, B. 2013, ApJ, 765, 47
Nestor, D. B., Shapley, A. E., Steidel, C. C., & Siana, B. 2011, ApJ, 736, 18
Osterbrock, D. E. 1989, Astrophysics of Gaseous Nebulae and Active Galactic Nuclei (Mill Valley, CA: University Science Books)
Ota, K., Iye, M., Kashikawa, N., et al. 2017, arXiv:1703.02501
Ouchi, M., Shimasaku, K., Akiyama, M., et al. 2008, ApJS, 176, 301
Ouchi, M., Shimasaku, K., Furusawa, H., et al. 2003, ApJ, 582, 60
Ouchi, M., Shimasaku, K., Furusawa, H., et al. 2010, ApJ, 723, 869
Pei, Y. C. 1992, ApJ, 395, 130
Pullen, A. R., Doré, O., & Bock, J. 2014, ApJ, 786, 111
Raiter, A., Schaerer, D., & Fosbury, R. A. E. 2010, A&A, 523, A64
Rauch, M., Haehnelt, M., Bunker, A., et al. 2008, ApJ, 681, 856
Reddy, N. A., Steidel, C. C., Pettini, M., Bogosavljević, M., & Shapley, A. E. 2016, ApJ, 828, 108
Robertson, B. E., Ellis, R. S., Furlanetto, S. R., & Dunlop, J. S. 2015, ApJL, 802, L19
Robertson, B. E., Furlanetto, S. R., Schneider, E., et al. 2013, ApJ, 768, 71
Rosdahl, J., & Blaizot, J. 2012, MNRAS, 423, 344
Sadoun, R., Zheng, Z., & Miralda-Escudé, J. 2017, ApJ, 839, 44
Schaerer, D. 2003, A&A, 397, 527
Schechter, P. 1976, ApJ, 203, 297
Schenker, M. A., Ellis, R. S., Konidaris, N. P., & Stark, D. P. 2014, ApJ, 795, 20
Shapley, A. E., Steidel, C. C., Pettini, M., & Adelberger, K. L. 2003, ApJ, 588, 65
Shimizu, I., & Umemura, M. 2010, MNRAS, 406, 913
Shull, J. M., Jones, J. R., Danforth, C. W., & Collins, J. A. 2009, ApJ, 699, 754
Silva, M. B., Santos, M. G., Gong, Y., Cooray, A., & Bock, J. 2013, ApJ, 763, 132
Sobral, D., Matthee, J., Best, P., et al. 2017, MNRAS, 466, 1242
Stark, D. P., Ellis, R. S., Chiu, K., Ouchi, M., & Bunker, A. 2010, MNRAS, 408, 1628
Steidel, C. C., Bogosavljević, M., Shapley, A. E., et al. 2011, ApJ, 736, 160
Trenti, M., Perna, R., & Jimenez, R. 2015, ApJ, 802, 103
Trenti, M., Perna, R., Levesque, E. M., Shull, J. M., & Stocke, J. T. 2012, ApJL, 749, L38
Verhamme, A., Orlitova, I., Schaerer, D., et al. 2017, A&A, 597, 13
Verhamme, A., Orlitová, I., Schaerer, D., & Hayes, M. 2015, A&A, 578, A7
Visbal, E., & Loeb, A. 2010, JCAP, 11, 016
Wise, J. H., Demchenko, V. G., Halicek, M. T., et al. 2014, MNRAS, 442, 2560
Wisotzki, L., Bacon, R., Blaizot, J., et al. 2016, A&A, 587, A98
Xue, R., Lee, K.-S., Dey, A., et al. 2017, ApJ, 837, 172
Yang, Y., Zabludoff, A. I., Davé, R., et al. 2006, ApJ, 640, 539
Zackrisson, E., Binggeli, C., Finlator, K., et al. 2017, ApJ, 836, 78
Zackrisson, E., Inoue, A. K., & Jensen, H. 2013, ApJ, 777, 39
Zhang, H., Zaritsky, D., Zhu, G., Ménard, B., & Hogg, D. W. 2016, ApJ, 833, 276
Zhao, D. H., Jing, Y. P., Mo, H. J., & Börner, G. 2009, ApJ, 707, 354
Zheng, Z., Cen, R., Trac, H., & Miralda-Escudé, J. 2010, ApJ, 716, 574
Zheng, Z., Cen, R., Trac, H., & Miralda-Escudé, J. 2011a, ApJ, 726, 38
Zheng, Z., Cen, R., Weinberg, D., Trac, H., & Miralda-Escudé, J. 2011b, ApJ, 739, 62